water

MDPI

Article

Deformation Monitoring and Potential Risk Detection of In-Construction Dams Utilizing SBAS-InSAR Technology—A Case Study on the Datengxia Water Conservancy Hub

Yi Ouyang [1,4], Tao Feng [1,4], Han Feng [2,*], Xinghan Wang [3], Huayu Zhang [1,4] and Xiaoxue Zhou [3]

1 State Grid Hunan Electric Company Limited Disaster Prevention and Reduction Center Changsha, Changsha 410000, China; oyy_0017@163.com (Y.O.); njuftao@126.com (T.F.); 18873235066@163.com (H.Z.)
2 Guizhou Provincial First Institute of Surveying and Mapping, Guiyang 550000, China
3 Pearl River Water Resources Research Institute, Pearl River Water Resources Commission, Guangzhou 510000, China; rsgiswxh@126.com (X.W.); zxx15116334982@163.com (X.Z.)
4 The State Key Laboratory of Disaster Prevention & Reduction for Power Grid, Changsha 410000, China
* Correspondence: ts18160001a31@cumt.edu.cn

Abstract: Deformation monitoring plays a pivotal role in assessing dam safety. Interferometric Synthetic Aperture Radar (InSAR) has the advantage of obtaining an extensive range of deformation, regardless of weather conditions. The Datengxia Water Conservancy Hub is the largest in-construction dam in China. To effectively assess the in-construction dam safety, the SBAS-InSAR (Small Baseline Subset-InSAR) technique and 86 Sentinel-1 images (from 11 February 2020, to 16 January 2023) have been employed in this study to monitor the deformation over the reservoir and its surrounding areas. The reliability of the SBAS-InSAR monitoring results over the study area was demonstrated by the in situ monitoring results. And the InSAR results show that the central section of the left dam exhibits the most substantial cumulative deformation, attributed to the maximal water pressure. This is closely followed by the left end of the dam, which reflects a similar but smaller deformation. However, the in-construction cofferdam facilities make the right-end section of the left dam more robust, and the deformation is the most stable. Additionally, significant deformation of the auxiliary dam slope has been identified. Moreover, the analysis indicated that the deformation of the four upstream slopes is closely related to the precipitation, which potentially poses a threat to the safety of the Datengxia Dam.

Keywords: Datengxia Water Conservancy Hub; SBAS-InSAR; deformation monitoring; time series analysis

Citation: Ouyang, Y.; Feng, T.; Feng, H.; Wang, X.; Zhang, H.; Zhou, X. Deformation Monitoring and Potential Risk Detection of In-Construction Dams Utilizing SBAS-InSAR Technology—A Case Study on the Datengxia Water Conservancy Hub. *Water* **2024**, *16*, 1025. https://doi.org/10.3390/w16071025

Academic Editor: Aristotelis Mantoglou

Received: 13 March 2024
Revised: 29 March 2024
Accepted: 30 March 2024
Published: 2 April 2024

1. Introduction

Water conservancy hub projects play a significant role in various aspects of society and the economy, encompassing flood control, water storage, irrigation, navigation, power generation, and more. However, over the prolonged operation of a dam, safety hazards can arise due to factors such as its structural integrity, geological composition, and the potential for surrounding landslides. In extreme cases, these issues can even pose threats to human lives and property. Therefore, it is imperative to provide scientific deformation monitoring data to enhance dam safety [1,2]. In comparison to traditional point-based survey methods such as Total Station, GPS, and Dumpy level [3–5], Spaceborne Synthetic Aperture Radar Interferometry (InSAR) technology boasts distinct advantages [6–8]. It offers the capability to acquire ground deformation information under all weather conditions, with high precision and across large spatial extents. This efficiency notably reduces the observation period, widens the spatial scope, and enhances monitoring accuracy [9–11], and is widely used for deformation monitoring, such as the deformation monitoring of landslides, volcanic activity, land subsidence, and other geological disasters [12,13].

With the development of InSAR technology, more and more researchers are exploring the use of InSAR for efficient and rapid dam safety monitoring. Wang Teng et al. (2011) utilized 40 SAR images, employing the PS InSAR and QPS InSAR methods to analyze the stability and deformation patterns of a concrete gravity dam during construction and operation [14]. Diego Di Martire (2014), using 51 ENVISAT-ASAR images find the high agreement between final InSAR displacements and in situ instrumental data, demonstrated the reliability of InSAR technique for the precise monitoring of civil infrastructures [15]. Pietro Milillo et al. utilized 198 COSMO SkyMed and TerraSAR-X image to conduct continuous 5-year monitoring on Italy's Pertusillo Dam, time series deformation derived by InSAR is highly correlated with ground deformation monitoring [16]. Wei Zhou used InSAR to observe the displacement properties of the Shuibuya Dam and found good agreement with results derived from the recorded internal monitoring data. The external monitoring results from the InSAR observation can be used as a supplement for traditional monitoring methods to analyze the parameters of the dam [17]. Al Husseinawi et al. (2018) assessed the stability of Iraq's Darbandikhan Dam post the 2017 Mw 7.3 Sarpol Zahab earthquake using 4 years of Sentinel-1 data [18–20]. Overall, the time series InSAR technology has been widely applied for monitoring reservoir dam deformation over time. The SBAS-InSAR method [21], as a representative time series InSAR technique, effectively overcomes the effects of temporal and spatial decorrelation and atmospheric delays by appropriately combining interferograms to analyze distributed scatterers (DSs) with high coherence. Research results from the application of SBAS-InSAR technology in dam monitoring [22–24] demonstrate that this technique can efficiently and accurately obtain deformation monitoring results for dams, allowing for real-time assessment of the dams' operational health status.

As a pivotal project in the Pearl River basin, the construction of the Datengxia Water Conservancy Hub began in 2014. The left dam was completed in January 2020, and the right dam is still under construction. It has been in service since January 2020, and has significantly contributed to flood control and water supply safety in the basin while fostering sustainable regional economic and social development [25]. Since its completion, the project has yielded remarkable economic, social, and environmental benefits. Before this study, no one had carried out large-scale deformation monitoring of the Datengxia Dam and the surrounding areas. Therefore, to ensure the secure operation of the dam during both construction and operation phases, using 86 Sentinel-1 satellite SAR images, as well as by using the Small Baseline Subset InSAR (SBAS InSAR) technique, this study conducted time series deformation monitoring over the Datengxia Water Control Project area. This study has obtained data related to the deformation of the Datengxia Dam, and simultaneously has identified potential landslide hazards and risks along both banks of the upstream Qianjiang River.

The remainder of this paper is organized as follows. Section 2 describes the study area and the data used. Section 3 is a description of the methodology and the workflow. Section 4 presents and analyzes the results. Eventually, the conclusion is given in Section 5.

2. Study Area and Data

2.1. Study Area

The Datengxia Water Conservancy Hub is situated in Guiping, Guangxi Province, China, and stands as the largest water conservancy undertaking within the Pearl River Basin. The geographical context of the study area is depicted in Figure 1. Encompassing a watershed region of approximately 198,600 km^2, the Datengxia Water Conservancy Hub covers 56.4% of the total area of the Xijiang River Basin. Its primary planning objectives include facilitating water storage for irrigation, implementing flood control measures across the watershed, improving navigational conditions, and ensuring a secure water supply for the Pearl River Delta and Macau. The hub primarily consists of the Qianjiang main dam and the Y-shaped Qianjiang auxiliary dam. The Qianjiang main dam takes the form of a concrete gravity dam, boasting a maximum dam height of 80 m and a dam length spanning 1343 m. On the left bank, the Qianjiang auxiliary dam features a clay core rock dam configuration with a dam length of 1239 m. The average elevation of the region encompassing the Datengxia Reservoir ranges between 23 and 43 m. During normal operational conditions, the reservoir's water level is maintained at 61 m, with a designed total storage capacity of approximately 3.43 billion cubic meters, in addition to a flood control storage capacity of roughly 1.5 billion cubic meters.

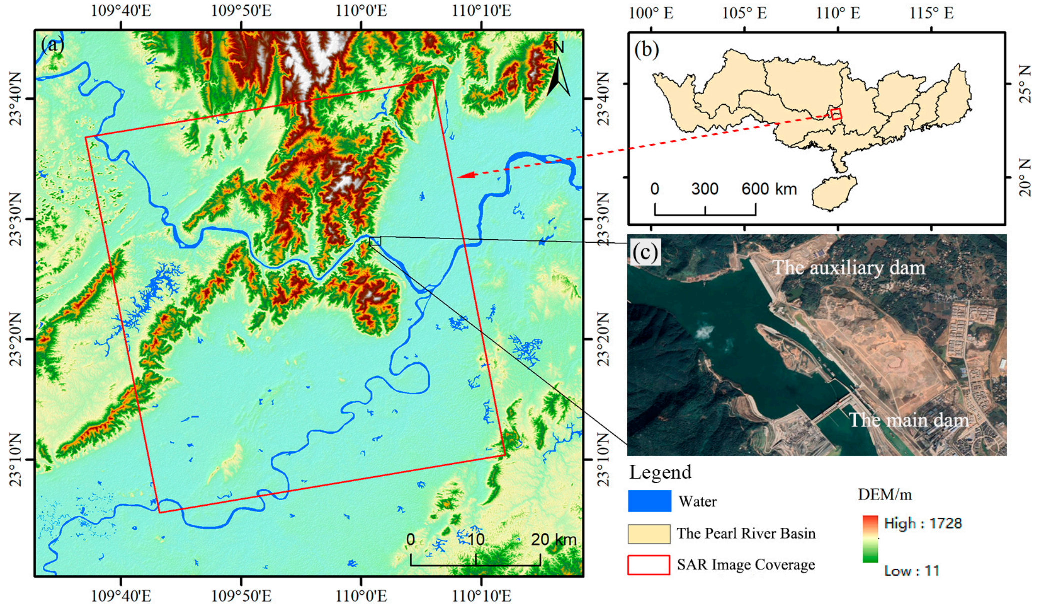

Figure 1. Overview of the study area. (**a**) Coverage of usage SAR data and DEM of the study area. (**b**) The Pearl River basin extent. (**c**) Datengxia Water Conservancy Hub, consists of a main dam and an auxiliary dam.

2.2. SAR Data

In this study, a total of 86 scenes of Sentinel-1 A satellite imagery were acquired from 11 February 2020 to 16 January 2023. To facilitate the monitoring, this research utilizes Synthetic Aperture Radar (SAR) data acquired through the Terrain Observation with Progressive Scans (TOPS) imaging mode of the satellite. The acquired image data exhibit azimuth and range resolutions of approximately 13.98 m and 2.33 m, respectively. Notably, these data are available for free download from the Sentinel Science Data Center of the European Space Agency. And we can see the detailed parameters in Appendix A.

Temporal Small Baseline Subset InSAR (SBAS-InSAR) methodology was employed to facilitate deformation monitoring in this study. Sentinel-1 satellite belongs to the C-band radar, and the control of the satellite orbit is very stable. To mitigate the temporal decorrelation effects due to seasonal vegetation changes, we chose a 62-day temporal threshold and 130 m spatial baseline to obtain better interferometric results, and the selected spatiotemporal baseline threshold is considered adequate to reduce the impact of the potential biases [26,27]. Consequently, a set of 222 interferograms was generated. The spatiotemporal baseline distribution of these interferometric pairs is depicted in Figure 2, from which we can see the temporal baseline is short and nearly 85% of the interferograms have spatial baselines below 100 m.

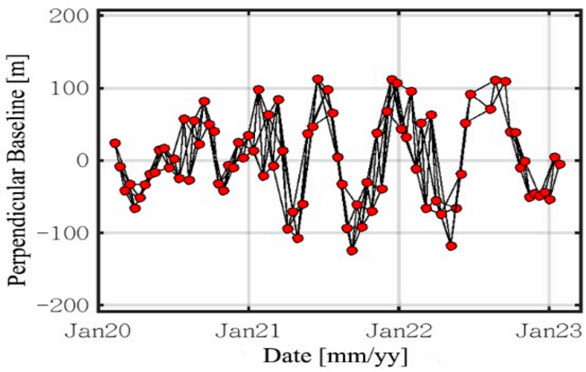

Figure 2. Spatiotemporal baseline distribution of 222 interferometric pairs. The red circles represent the Sentinel−1 acquisitions, and the black lines indicate the combination of the interferometric pairs.

3. Methods

3.1. Data Preprocessing

The pre-processing workflow for raw SAR data can be seen in Appendix B, which comprises four steps: orbit refinement, Single-Look Complex (SLC) images extraction, high-precision registration, and multi-look cropping.

Incorporating Precise Orbit Ephemeris Information: In the InSAR processing workflow, accurate precise orbit data integration is crucial. Precise orbit information serves a dual purpose: aiding geometric registration algorithms in achieving high-precision alignment of SAR images and effectively removing residual systematic orbit errors within the interferometric phase. Typically, after downloading Sentinel-1 data, we use precision orbit ephemeris data files to format into single-look complex (SLC) images.

Extraction of swaths and bursts within the study area: The Sentinel-1 satellite employs the Terrain Observation by Progressive Scans (TOPS) imaging mode [28]. During its flight, the radar beam oscillates and sweeps from rear to front along the azimuth direction, sequentially gathering data from three mapping swaths. The radar beam is also divided into multiple bursts within each mapping swath to maintain consistent image quality. Neighboring bursts are amalgamated based on the research area for coherent interferometric processing. For this study, the Datengxia Gorge-centered study area comprises 1 to 3 bursts sourced from the third mapping swath.

High-precision registration: High-precision SLC registration is fundamental to InSAR interferometry. Sentinel-1's TOPS mode alters beam coverage rapidly during each set of burst scans, inducing Doppler frequency shifts along the azimuth. This necessitates heightened registration precision to mitigate phase discrepancies. Accurate interferograms require interference phase deviation within the image under 3 degrees, necessitating azimuth registration accuracy finer than one-thousandth of a pixel [29]. In the processing workflow, SAR data captured on 17 February 2021 were designated as the primary image for registration preprocessing. Initial alignment is achieved via geometric registration, followed by fine registration using the spectral diversity method. This approach achieves registration precision down to one-thousandth of a pixel.

Study area cropping and multi-look processing: The registered SLC is systematically cropped to align with the designated research area. Subsequently, a multi-look processing strategy is applied, maintaining a 4:1 multi-look ratio in both the range and azimuth dimensions. While this might reduce spatial resolution, multi-look processing reduces noise and harmonizes spatial resolution across dimensions [30]. This congruence in spatial resolution facilitates subsequent processing tasks.

3.2. SBAS InSAR Processing

The flowchart of InSAR data processing for small baseline set timing is shown in Figure 3. After data preprocessing, to improve the coherence of image interference, we selected image sets with shorter spatiotemporal baselines in N + 1 images and then connected them in pairs, generated interferograms [21]. Next, we identified and selected all potential candidate monitoring points. Then, we corrected the DEM error and performed the 3-D phase unwrapping. Finally, in the deformation solution process, singular value decomposition (SVD) was used to solve the problem of matrix rank deficiency caused by multi-master images, so as to obtain the deformation unique solution under the minimum norm criterion [21,31,32]. Below is a brief explanation of the principle of this technology.

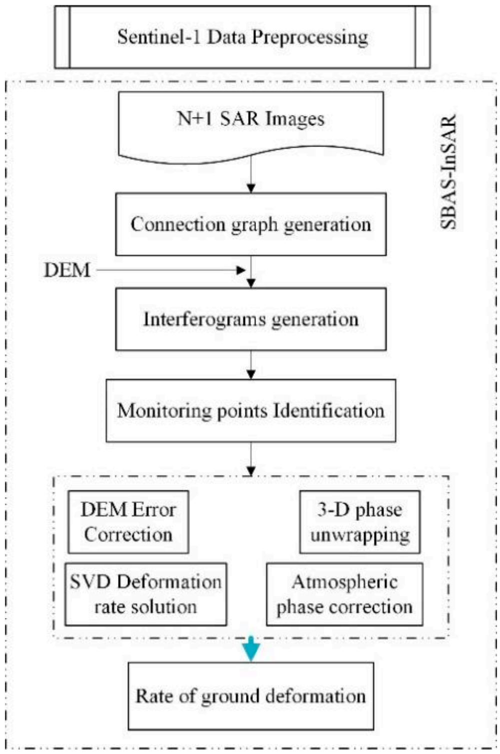

Figure 3. Flow chart of SBAS-InSAR data processing.

Assuming there are $(t_0, t_1, t_2, \cdots, t_N)$ a total of $N + 1$ temporal SAR images, after registering all images in the same geometric space, the interference pairs are organized according to the principle of short spatiotemporal baseline. If at least one SAR image interferes with it in each period, then $(N + 1)$ SAR images can form M interference pairs, and M meets the following conditions:

$$\frac{N+1}{2} \leq M \leq \frac{N(N+1)}{2} \tag{1}$$

For the jth scene differential interferogram generated by t_1 and t_2 image interference, the differential interference phase $\delta\varnothing_j$ (ignoring atmospheric error phase, residual terrain phase, and noise) can be expressed as:

$$\delta\varnothing_j = \varnothing_2(x,r) - \varnothing_1(x,r) \approx \frac{4\pi}{\lambda}[\mathrm{d}(t_2,x,r) - \mathrm{d}(t_1,x,r)] \tag{2}$$

In the formula, $\varnothing$ is the interference phase; λ is the central wavelength of the signal; $\mathrm{d}(t_B,x,r)$ and $\mathrm{d}(t_A,x,r)$ are the cumulative shape variables of the radar line of sight under t_2 and t_1 spatial positions, respectively.

The phase in the above equation can be expressed as the product of the average phase velocity v_i of any two acquisition times and time, i.e.,

$$v_i = (\phi_i - \phi_{i-1})/(t_i - t_{i-1}) \tag{3}$$

The $\delta\varnothing_j$ of the jth scene differential interferogram, which generated by t_1 and t_2 image, can be written as:

$$\delta\varnothing_j = \sum_{t_1,i}^{i,t_2}(t_i - t_{i-1})v_i \tag{4}$$

Therefore, the differential interference phase of each time period can be written as:

$$\delta\varphi = Bv \tag{5}$$

The differential interference phase vector $\delta\varphi$ obtained by three-dimensional unwrapping of the representative phase [33,34]; the deformation parameters φ are to be solved; A represents a coefficient matrix related to the organizational form of interference, and the rank deficiency of this matrix is closely related to the form of the small baseline set.

In order to obtain the surface deformation variables $\varphi_{m,n}$ within the time interval, the deformation phase is converted into the product of the average phase velocity $v_{n,m}$ of the interference pair within the time interval and time $t_{n,m}$, and the average phase velocity $\hat{v}$ is converted to the average deformation rate $\mathrm{V}_{\mathrm{velocity}}$ by Equation (8), λ is the radar wavelength:

$$A\varphi = Bv = \delta\varphi \tag{6}$$

$$\hat{v} = \left(B^T B\right)^{-1} B^T \delta\varphi \tag{7}$$

$$\mathrm{V}_{\mathrm{velocity}} = \lambda\hat{v}/2\pi \tag{8}$$

Generally, coefficient matrix B is a rank deficient matrix with rank $M - N + 1$, and M is the number of interference pairs. It is necessary to use the SVD method to obtain the generalized inverse matrix of matrix B, and then obtain the minimum norm solution of the speed vector. Finally, the shape variables of each time period can be obtained by integrating the speed of each time period.

3.3. Covert the In-Suit Monitoring Results to Radar LOS Direction

In this study, we use the in-suit monitoring results measured by Leica TM5 Georobots to validate InSAR-derived results. Since the deformation detected by InSAR is along the line-of-sight (LOS), we need to convert the in-suit monitoring results to the LOS direction for the comparison, and we used the following equation for this projection:

$$\mathrm{d}_{los} = cos\alpha sin\vartheta d_e - sin\alpha cos\vartheta d_n - cos\vartheta d_u \tag{9}$$

where d_e, d_n, d_u, are displacements in east, north, and vertical direction, respectively, α is the azimuth of the satellite heading, and ϑ is the radar incidence angle. More details can be found in [17].

4. Results and Discussion

4.1. Average Deformation Rate of the Study Area

Following the processing methodology outlined in Section 2, we used a combination of small baselines to generate interferograms, after which Goldstein filtering was implemented to improve the phase stability. Figure 4 illustrates interferograms from multiple periods; the quality of interference fringes in autumn and winter is better. However, even though we adopt the SBAS strategy to generate the interferograms, the three interferograms b, e, and h are still affected by temporal decorrelation in the summer. The temporal decorrelation is due to the rapid growth of vegetation in the summer, and the C-band radar on the Sentinel-1 satellite has poor penetration ability of vegetation, resulting in unclear interference fringes.

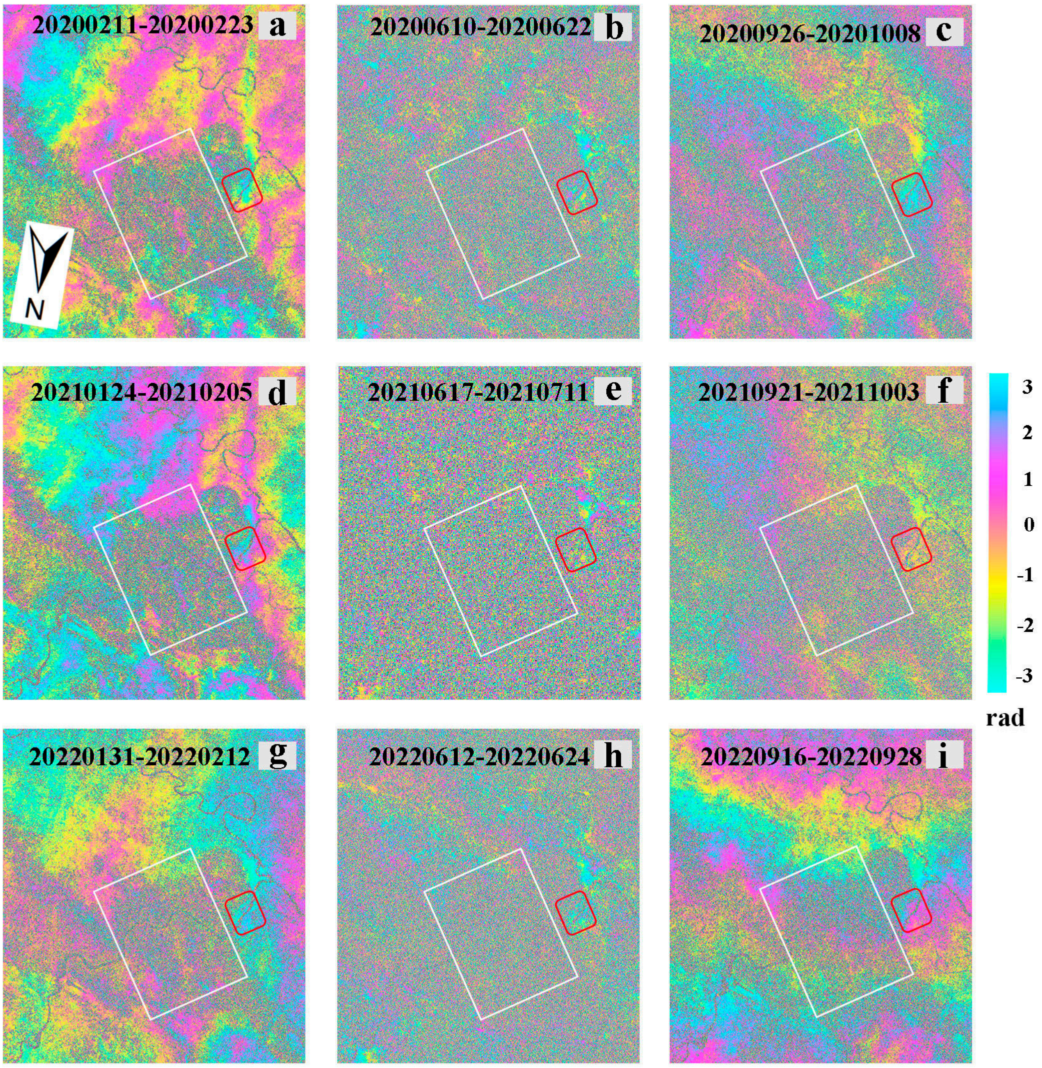

Figure 4. Comparison of differential interferograms from multiple periods: (**a**–**c**) are interferograms from February, June, and September 2020; (**d**–**f**) are interferograms from February, June, and September 2021; and (**g**–**i**) are interferograms from February, June, and September 2022. The red rectangle represents dam area, and the white rectangle represents mountainous regions.

After phase unwrapping, atmospheric error removal, and residual topography error phase correction [35–37], the line-of-sight (LOS) direction deformation was obtained, as Figure 5 shows. Notably, Figure 5 exhibits a scarcity of monitoring points along the riverbanks (marked by white square). This limitation arises from the characteristics of the Sentinel-1 satellite, which operates in the C-band. The C-band has a shorter wavelength and limited penetration through vegetation. As a result, areas with vegetated mountainous terrain along the riverbanks exhibit diminished interference coherence, leading to a sparse distribution of highly coherent monitoring points. This phenomenon can also be demonstrated from the interferograms in Figure 4, where the fringes in vegetated mountainous area (also marked by white squares in Figure 4) are not very clear because of the intrinsic defects in C-band radar. Conversely, in the area where the dam is located (marked by red squares in Figures 4 and 5), relatively even terrain and less vegetation are characterized by numerous high-coherence pixels, so there is a clear interference fringe here, leading to the concentration of monitoring points and an overall effective monitoring outcome. Similarly, in the lower half of the image, regions with a significant concentration of artificial structures exhibit a high density of monitoring points and distinct interference fringes, which are well maintained.

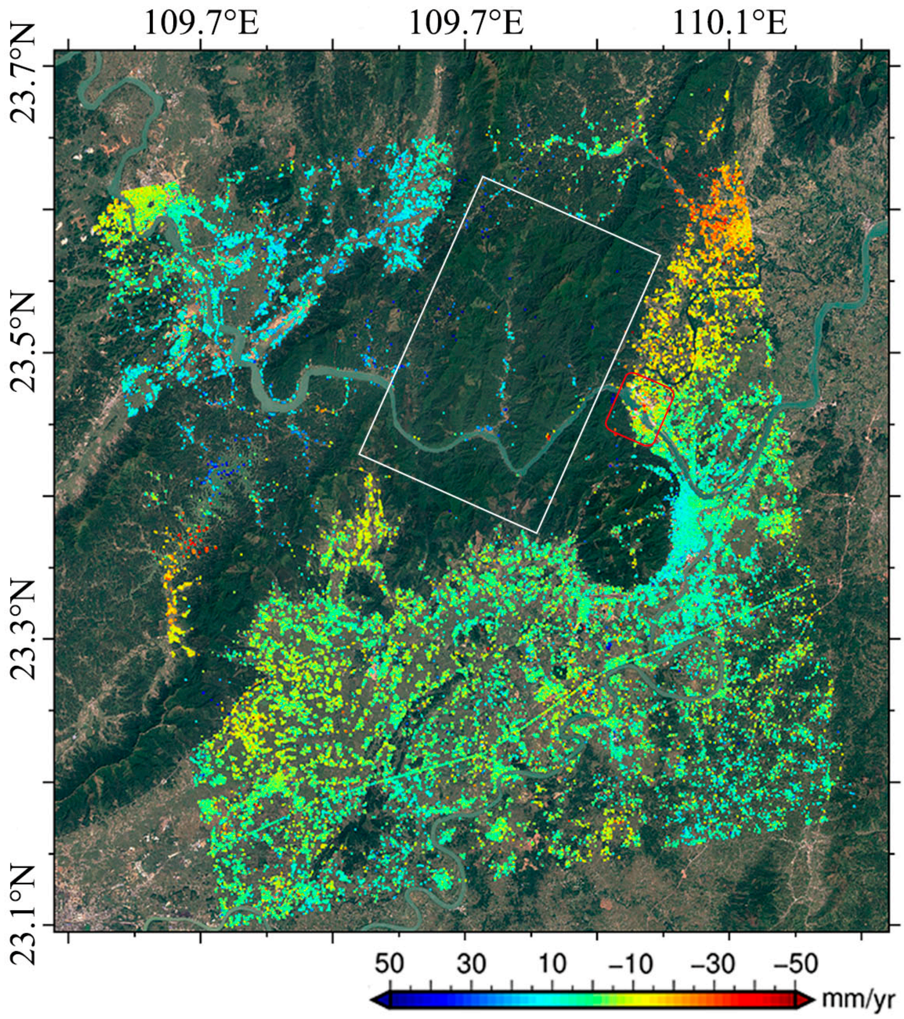

Figure 5. Average deformation rate over the study area. The red rectangle represents dam area, and the white rectangle represents mountainous regions.

Additionally, Figure 5 demonstrates a state of relative stability across the study area. The deformation in urban conglomerations range is within ±10 mm. Subsequent sections will delve into a comprehensive exploration and analysis of the time series deformation related to the primary structure of the Datengxia Dam, as well as the slopes adjacent to the riverbanks.

4.2. Time Series Deformation Analysis of the Main Dam of Datengxia

In the same way as all artificial construction, the dam and construction area prominently exhibit a robust radar wave reflection signal, rendering it clearly identifiable as distinct bright features with discernible textural attributes in SAR images. Because of the stable strongly reflected signal of such artificial construction, InSAR can easily detect more monitoring points. Figure 6 shows SAR images of the Datengxia Dam, captured in January 2021, March 2022, and October 2022. In these SAR images, dark areas signify bodies of water, while brighter areas correspond to the finalized dam (prominently illuminated linear structures in the middle of images) and artificial construction area (bright surface clusters in the bottom and left part of images). By leveraging optical images and multi-temporal SAR images spanning September 2021, it becomes evident that over the course of the monitoring period, the left dam within the Datengxia Water Control Project was brought to completion. Simultaneously, the right dam (highlighted in yellow, indicative of its ongoing construction) approached substantial completion by the close of 2022, and was fully completed in June 2023, culminating in noteworthy surface alterations.

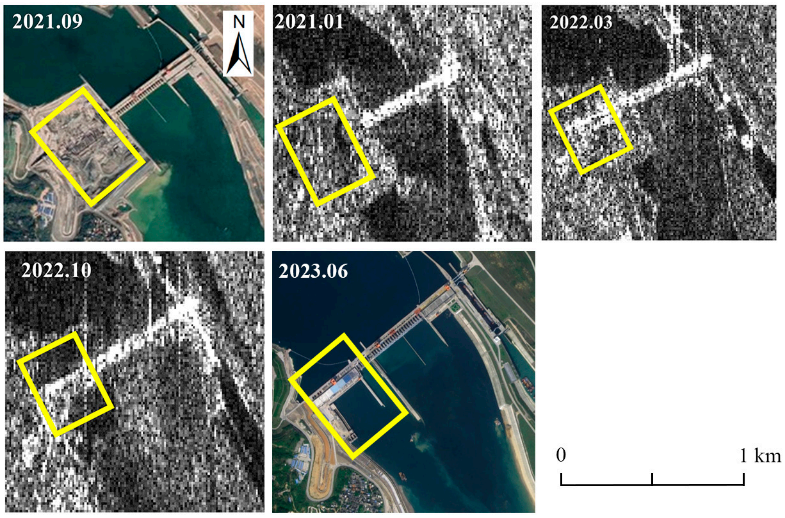

Figure 6. Time series image of the in-construction Datengxia Dam.

As presented in Figure 7, along the water flow direction, the left dam of Datengxia exhibits a significant concentration of highly coherent monitoring points. Conversely, the monitoring points over the right dam region are notably sparse. The rationale underlying this discrepancy can be deduced from the conclusions drawn from the multi-temporal SAR image analysis concerning the right dam of Datengxia, as evidenced in Figure 6. The scarcity of monitoring points in the right dam area can be attributed to the rapid surface alterations induced by the construction of the cofferdam zone throughout the monitoring duration. These alterations engendered interference and subsequently disrupted coherence within this specific region, thereby contributing to the dearth of highly coherent deformation monitoring points. However, on an overarching basis, the utilization of C-band Sentinel1 imagery for undertaking time series InSAR deformation monitoring of the Datengxia Dam is validated as both effective and feasible.

InSAR deformation monitoring is widely used in dam structure analysis [38,39]. Even though InSAR technology will be affected by multiple error sources, these errors can be weakened by fine, time series InSAR processing, and monitoring accuracy can still reach the centimeter level [40–43]. In this study, the SBAS InSAR-derived results have been validated by a Georobot Deformation Monitoring System. The locations of the Georobots are shown in Figure 7 (marked by three pentagons), and their deformation values from 8 March 2020 to 13 April 2021 were measured by Leica TM5 electronic total station, depicted in Figure 8.

The Figure 8 shows the time series deformation derived by InSAR (2020–2023) and the deformation measured by Georobots (the deformation values had converted to the InSAR LOS direction by the method in Section 3.3). From Figure 8, we can find that the InSAR monitoring deformation results are consistent with the in situ results, and the difference between the two technologies is small in magnitude, with an accuracy of around a few millimeters. Therefore, the InSAR deformation monitoring results are reliable. It is worth mentioning that the TPB1 point on the slope exhibits some deformation following the in situ monitoring period.

To further analyze the temporal deformation features of the Datengxia Dam, eight areas (marked by circle in Figure 7) on the dam were selected for temporal analysis, and the results are shown in Figure 9.

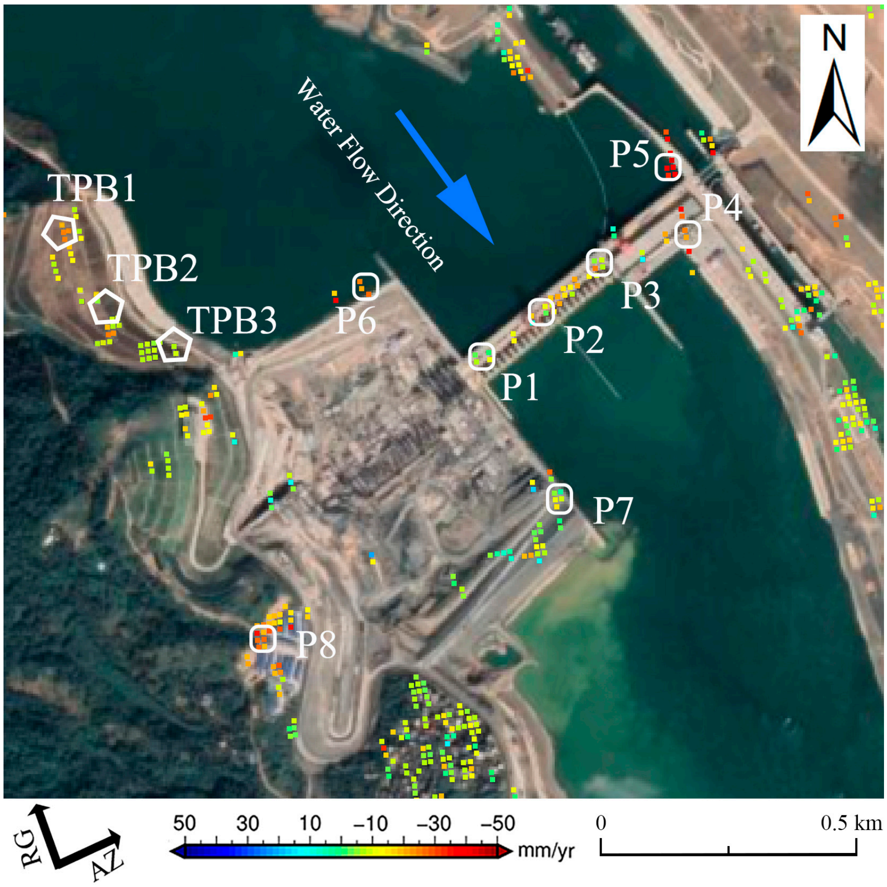

Figure 7. The deformation velocity of the Datengxia Dam. P1, P2, P3, P4, and P5 are located in the left dam; P6 and P7 are on the right dam; P8 is on the right bank slope; TPB1, TPB2, TPB3 are where the Georobots are located. RG represents Range Distance, and AZ represents Azimuth.

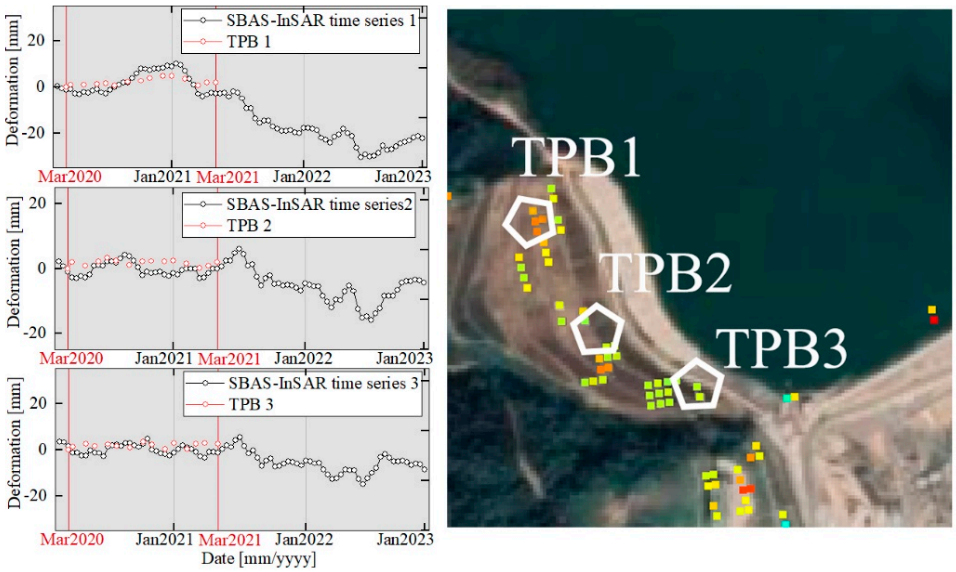

Figure 8. Comparison between the InSAR monitoring deformation and the Georobot deformation monitoring results.

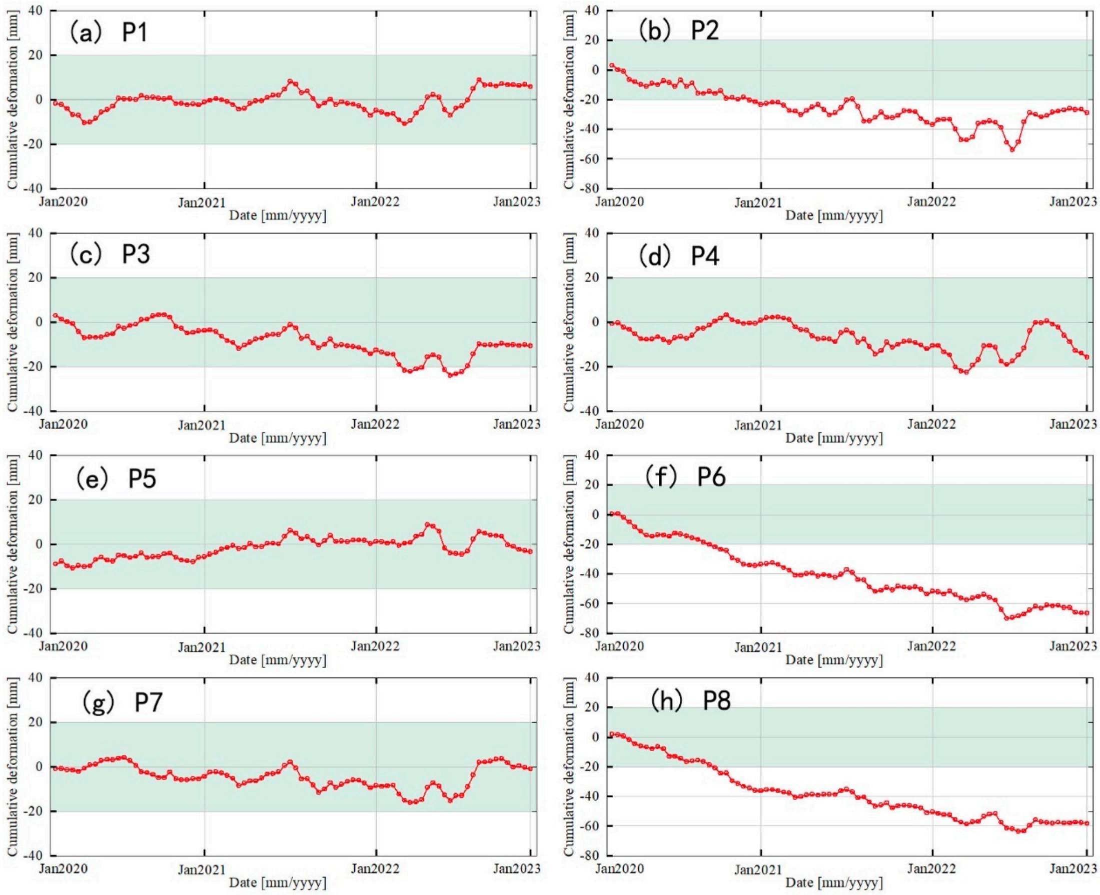

Figure 9. Cumulative deformation of typical areas over Datengxia Dam. P1, P2, P3, P4, P5 are situated on the left dam. P6 and P7 are located at the right dam, and P8 is at the right slope.

As depicted in Figure 8, P1, P2, and P3 are situated within the core of the left dam's main structure. The cumulative temporal deformation of these three regions is depicted in Figure 9a, Figure 9b, and Figure 9c, respectively. The results reveal that over the 3-year monitoring period, the temporal deformation in the P1 region oscillates within the range of −20 to 20 mm, ultimately amounting to a cumulative deformation nearing 5 mm. Likewise, the temporal deformation realm encompassing the P2 region varies from −60 to 20 mm, ultimately yielding a cumulative deformation extending approximately −30 mm over the 3-year duration. Concurrently, the temporal deformation in the P3 region fluctuates between −20 and 20 mm, coalescing into a cumulative deformation nearing −10 mm. Notably, situated at the center of the left dam's primary structure, the P2 region experiences the maximal influence from reservoir water pressure, consequently incurring the most substantial cumulative temporal deformation, the amount of subsidence increases from the outer border of the left dam to the middle [44]. This is closely followed by the P3 regions, reflecting a similar trend. Notably, although P1 and P3 are at both ends of the left dam, the deformation trend of P3 is more obvious than P1 during the monitoring period. According to the in-construction right dam in Figure 7, we think this is due to the fact that P1 is at the junction of the right in-construction cofferdam facilities, which provides some support to P1 area and makes it more robust. Therefore, compared to the P3 without such a robust structure, the deformation of the P1 region is more stable during the monitoring period, and almost stable at around 0 mm. In the broader context, the cumulative deformation exhibited by these three areas over the 3-year monitoring period remains relatively modest. Overall, these findings collectively underscore the overarching stability of the left dam structure.

The P4 and P5 areas are located in the Datengxia shiplock area, and their temporal deformation is shown in Figure 9d,e. The deformation of the P4 and P5 areas is stable, ranging from −20 to 20 mm, but with fluctuations. This phenomenon is due to the large number of wall facades in the area, which form many dihedral reflectors, and the strong signal interference brought by the strong dihedral scattering leads to abnormal fluctuations in InSAR monitoring deformation.

The P6 and P7 areas are located on the cofferdam water retaining facilities of the right dam construction. The temporal deformation of this area is shown in Figure 9f,g. The results show that the accumulated deformation in the P6 area is relatively large, about 65 mm, while the deformation in the P7 area is basically around 0 mm. The reason for this is because point P6 is located on the water blocking facilities upstream of the river, directly bearing a large amount of reservoir water pressure, resulting in significant deformation in the p6 area. However, due to its location downstream of the river, point P7 does not directly bear reservoir water pressure, resulting in relatively stable deformation.

The P8 area represents a slope on the right bank, and the temporal deformation is shown in Figure 9h. The results show that since 2020, the region has experienced a cumulative deformation of about 60 mm, with a clear trend of linear deformation and a relatively high level of risk, which deserves more attention.

4.3. Deformation Analysis of River Bank Slopes

The deformation on both banks of the upstream of the Qianjiang River is shown in Figure 10 (area is indicated by a white box on the left side). According to the deformation monitoring results, during the monitoring period from 2020 to 2023, there are four obvious deformation areas: A1, A2, A3, A4. The distribution of each area is shown in Figure 10.

The average deformation of A1, A2, A3, and A4 areas reaches around 60 mm, 60 mm, 70 mm, and −60 mm (Figure 10a), respectively. Except for the negative average deformation rate of A4, the average deformation rate of the other three deformation areas is positive. This is due to the side view imaging method adopted by SAR satellites. The deformation monitored is along the line of sight (LOS) direction of the satellite sensor, and the actual downward deformation of slopes projected on the satellite line of sight may appear as negative deformation (away from satellite sensor) or positive deformation (towards satellite sensor) [45]. Overall, there is obvious deformation in all the four areas, and the deformation also shows a linear trend, which is suspected to be a sign of landslide activity.

To explore the inducing factors of the deformations, we analyzed the relationships between the precipitation and the times series deformation. Since the time span of the SAR images (11 February 2020–16 January 2023), the precipitation data were processed according to the temporal baseline length between the SAR images, which makes the analysis more reasonable. Figure 10b–e illustrate the time series deformation of the four areas and their relationship with precipitation.

As the figures show, the precipitation was mostly concentrated in May to September each year. Therefore, in this study, the concentrated precipitation period from 2020 to 2023 is noted by dashed boxes, and from the green dashed boxes in Figure 11, we can obviously find that the deformation of each area accelerated during the concentrated precipitation period, indicating that precipitation was an important factor leading to the deformation acceleration. As with the concentrated precipitation period in 2020, there was accelerated uplift in the A1, A2, A3 areas, and accelerated settlement deformation in the A4 area, and all four regions present significant accelerated deformation trends. Similarly, in 2021 and 2022, the deformation of all four regions showed the same accelerating trend characteristics caused by the rainy weather, indicating that the deformation of the four regions was more related to rainfall. An interesting phenomenon is that the A4 area did not immediately experience accelerated deformation in 2022. We think it is because the stability of the slope was destroyed to a certain extent, and after continuous rainfall, the accelerated deformation occurred due to other factors such as gravity. Moreover, in Figure 10, the precipitation in 2021 was less than that in 2020 and 2023, so the deformation acceleration is not significant. Overall, in these areas, extremely rainy weather and concentrated precipitation are the major inducing factors for accelerated surface deformation.

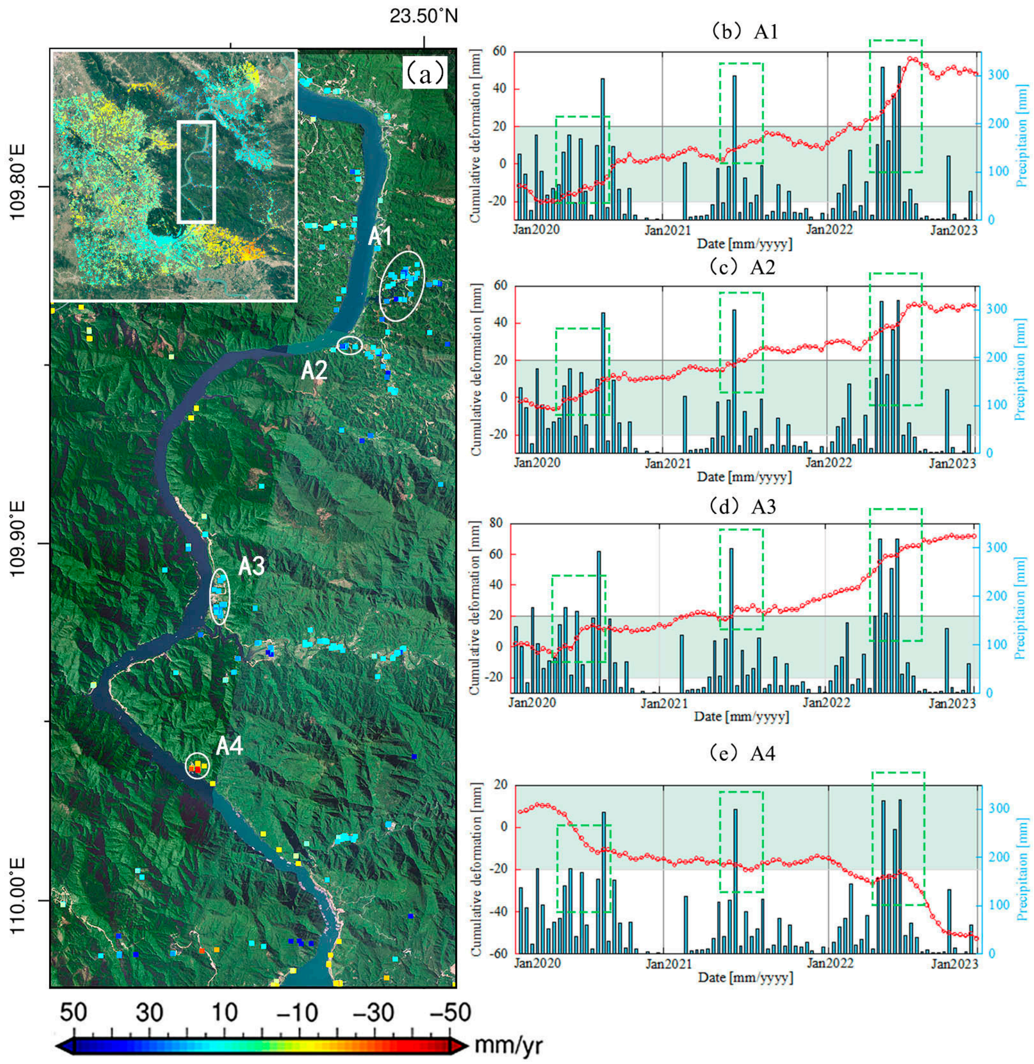

Figure 10. Average deformation rate and cumulative deformation of the upper reaches of Datengxia Dam: (**a**) shows four obvious deformation slope areas; and (**b**–**e**) illustrate the time series deformation of the four areas and their relationship with precipitation. Green dashed boxes in (**b**–**e**) highlight the periods of concentrated precipitation.

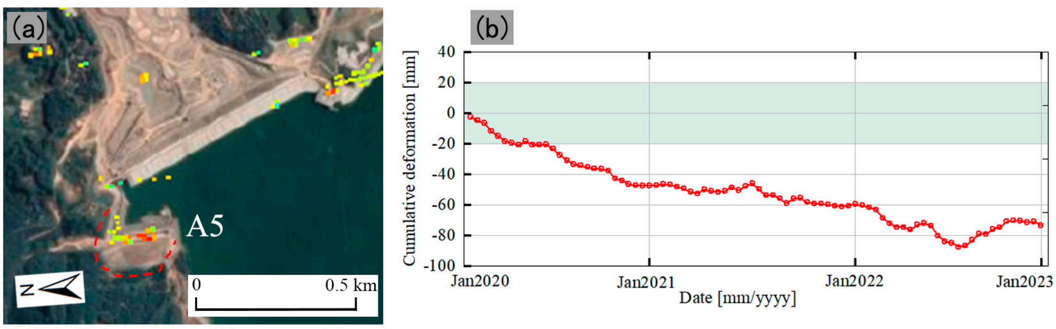

Figure 11. Deformation monitoring result of the auxiliary dam: (**a**) average deformation rate, the deformation rate color is the same as in Figure 10; and (**b**) cumulative deformation.

Furthermore, it is important to highlight the presence of a reservoir slope exhibiting significant deformation. This slope is situated near the auxiliary dam (the geographical location can be seen in Figure 1), approximately 2 km away from the main dam of the Datengxia. See Figure 11 for the deformation monitoring results. From Figure 11a, it can be seen that the average deformation rate monitored by InSAR in the A5 region is relatively high, about 30 mm/y. Figure 11b also shows that the cumulative deformation over the A5 region has reached to about 80 mm, and the linear trend of deformation is obvious, indicating that it may have a high landslide risk or pose a certain threat to the auxiliary dam and even the main dam of the Datengxia Reservoir. Therefore, it is necessary to pay more attention to the deformation in the A5 region in the future.

5. Conclusions

In this study, by employing the SBAS-InSAR method and Sentinel-1 data, the deformation over the Datengxia Water Conservancy Hub and its surrounding areas has been obtained and analyzed. Specifically, 86 Sentinel-1 images acquired from February 2020 to January 2023 were used to generate the 222 small baseline interferograms for the monitoring. Based on the time series deformation over the study area for nearly 3 years, the deformation characteristics of eight typical subareas have been analyzed, and potentially at risk slopes along the riverbanks have been identified. The main findings of this study are as follows:

(1) The utilization of SBAS-InSAR technology together with Sentinel-1 imagery has facilitated the accomplishment of time series deformation monitoring over the Datengxia reservoir. By comparison with the in situ data, the SBAS-InSAR monitoring results have been proved to be reliable and effective. However, the limitations inherent in Sentinel-1 data, i.e., the shorter wavelength and low resolution, result in sparser monitoring points over densely vegetated mountainous areas. Using high-resolution, long-wavelength SAR datasetss in collaboration with other geodetic techniques would be an effective solution for this problem;

(2) Due to the maximal water pressure, the central section of the dam exhibits the most substantial cumulative deformation, approximately 30 mm. Furthermore, the left end of that dam reflects a similar but smaller deformation, coalescing into a cumulative deformation nearing −10 mm. However, the in-construction cofferdam facilities make the right-end section of the left dam more robust, and the deformation is the most stable and almost always stable at around 0 mm. Overall, the deformation results demonstrate the stability of the main structure of the left dam. Additionally, a notable deformation slope near the right dam has experienced a cumulative deformation of about 60 mm, showing a clear trend of linear deformation and a relatively high level of risk;

(3) Four distinct slopes exhibiting linear deformation trends along the banks have been recognized, and the correlation analysis of the four slopes' deformation time series with the rainfall suggests their deformation is mainly affected by precipitation. Furthermore, a reservoir slope within the auxiliary dam precinct has also exhibited a significant deformation, with the cumulative deformation of approximately 80 mm, thus, more attention should be paid to its stability.

Author Contributions: Conceptualization, H.F. and Y.O.; methodology, H.F., T.F. and Y.O.; validation, X.W., H.Z. and X.Z.; results analysis, H.F. and X.W.; writing—review and editing, Y.O. and H.F.; visualization, X.W.; supervision, T.F. and Y.O. All authors have read and agreed to the published version of the manuscript.

Funding: This research was funded by the State Grid Major S&T Project (grant number 5200-202322139A-1-1-ZN).

Data Availability Statement: Data incorporated in this research are freely available through these webpages: Sentinel-1A (https://dataspace.copernicus.eu/), S1 satellite precise orbit data (https://s1qc.asf.alaska.edu/aux_poeorb/). Daily precipitation data were obtained from the National Meteorological Information Centre of the China Meteorological Administration (https://data.cma.cn/).

Acknowledgments: The authors would like to thank the free Sentinel-1 data provided by the European Space Agency. The authors would also like to thank Zhao Feng of China University of Mining and Technology for his guidance of this paper.

Conflicts of Interest: Yi Ouyang, Tao Feng and Huayu Zhang were employed by the State Grid Hunan Electric Company Limited Disaster Prevention and Reduction Center; Xinghan Wang and Xiaoxue Zhou were employed by Pearl River Water Resources Research Institute, Pearl River Water Resources Commission, and Han Feng was employed by GuiZhou Provincial First Institute of Surveying and Mapping. All authors declare that the research was conducted in the absence of any commercial or financial relationships that could be construed as a potential conflict of interest.

Appendix A

The following table lists the detailed parameters of the Sentinel-1 satellite:

Parameter	Value
Frame	72
Path	157
Angle of flight direction	−10.19 (°)
Incident angle	43.98 (°)
Range resolution	2.33 (m)
Azimuth Resolution	13.99 (m)
Wavelength	5.55 (cm)
Collection time	10:50 UTC

Appendix B

The pre-processing workflow for Sentinel-1 SAR data:

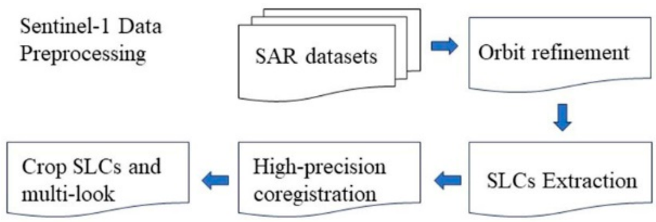

References

1. Szostak-Chrzanowski, A.; Chrzanowski, A.; Massiéra, M. Use of deformation monitoring results in solving geomechanical problems—Case studies. *Eng. Geol.* **2005**, *79*, 3–12. [CrossRef]
2. Hunter, G.; Fell, R. *The Deformation Behaviour of Embankment Dams*; The University of New South Wales: Sydney, Australia, 2003; ISBN 978-0-85841-383-2.
3. He, X.; Hua, X.; Ding, X.; Chen, Y.; Sun, Y. Development of GPS Multi-antenna based deformation monitoring system. *Hydropower Autom. Dam Monit.* **2002**, *26*, 34–36. (In Chinese)
4. Cui, P. Research on Dam Safety Monitoring Based on GNSS and Measuring Robots:A Case Study of the Pillow Dam Hydropower Station. *Yangtze River* **2020**, *51*, 132–134. (In Chinese)
5. Kalkan, Y. Geodetic deformation monitoring of Ataturk Dam in Turkey. *Arab. J. Geosci.* **2012**, *7*, 397–405. [CrossRef]
6. Wang, R.; Yang, T.; Yang, T.; Liao, M. A safety analysis of elevated highways in Shanghai linked to dynamic load using long-term time-series of InSAR stacks. *Remote Sens. Lett.* **2019**, *10*, 1133–1142. [CrossRef]
7. Gili, J.A.; Moya, J.; Corominas, J.; Crosetto, M.; Monserrat, O. Past, Present and Future Monitoring at the Vallcebre Landslide (Eastern Pyrenees, Spain). *Appl. Sci.* **2021**, *11*, 571. [CrossRef]
8. Wang, T.; Perissin, D.; Rocca, F.; Liao, M.-S. Three gorges dam stability monitoring with time-series InSAR image analysis. *Sci. China Earth Sci.* **2011**, *54*, 720–732. [CrossRef]
9. Zhao, F.; Wang, T.; Zhang, L.; Feng, H.; Yan, S.; Fan, H.; Xu, D.; Wang, Y. Polarimetric Persistent Scatterer Interferometry for Ground Deformation Monitoring with VV-VH Sentinel-1 Data. *Remote Sens.* **2022**, *14*, 309. [CrossRef]
10. Liu, J.; Wang, Y.; Yan, S.; Zhao, F.; Li, Y.; Dang, L.; Liu, X.; Shao, Y.; Peng, B. Underground coal fire detection and monitoring based on Landsat-8 and Sentinel-1 data sets in Miquan fire area, XinJiang. *Remote Sens.* **2021**, *13*, 1141. [CrossRef]
11. Wang, T.; Wang, Y.; Zhao, F.; Feng, H.; Liu, J.; Zhang, L.; Zhang, N.; Yuan, G.; Wang, D. A spatio-temporal temperature-based thresholding algorithm for underground coal fire detection with satellite thermal infrared and radar remote sensing. *Int. J. Appl. Earth Obs. Geoinf.* **2022**, *110*, 102805. [CrossRef]

12. Zhao, C.; Lu, Z.; Zhang, Q.; Juan, F. Large-area landslide detection and monitoring with ALOS/PALSAR imagery data over Northern California and Southern Oregon, USA. *Remote Sens. Environ.* **2012**, *124*, 348–359. [CrossRef]
13. Wang, B.; Zhao, C.; Zhang, Q.; Peng, M. Sequential InSAR Time Series Deformation Monitoring of Land Subsidence and Rebound in Xi'an. *China Remote Sens.* **2019**, *11*, 2854. [CrossRef]
14. Wang, T.; Perissin, D.; Rocca, F. Stability Monitoring of the Three Gorges Dam Based on Time Series SAR Image Analysis Method. *Sci. China Earth Sci.* **2011**, *41*, 110–123.
15. Di Martire, D.; Iglesias, R.; Monells, D.; Centolanza, G.; Sica, S.; Ramondini, M.; Pagano, L.; Mallorquí, J.J.; Calcaterra, D. Comparison between Differential SAR interferometry and ground measurements data in the displacement monitoring of the earth-dam of Conza della Campania (Italy). *Remote Sens. Environ.* **2014**, *148*, 58–69. [CrossRef]
16. MacChiarulo, V.; Milillo, P.; Blenkinsopp, C.; Reale, C.; Giardina, G. Multi-temporal InSAR for transport infrastructure monitoring: Recent trends and challenges. *Proc. Inst. Civ. Eng. Bridge Eng.* **2021**, *176*, 92–117. [CrossRef]
17. Zhou, W.; Li, S.; Zhou, Z.; Chang, X. Insar observation and numerical modeling of the earth-dam displacement of shuibuya dam (China). *Remote Sens.* **2016**, *8*, 877. [CrossRef]
18. Dong, S.; Yin, H.; Yao, S.; Zhang, F. Detecting surface subsidence in coal mining area based on DInSAR technique. *J. Earth Sci.* **2013**, *24*, 449–456. [CrossRef]
19. Li, T.; Motagh, M.; Wang, M.; Zhang, W.; Gong, C.; Xiong, X.; He, J.; Chen, L.; Liu, J. Earth and rock-filled dam monitoring by high-resolution X-band interferometry: Gongming dam case study. *Remote Sens.* **2019**, *11*, 246. [CrossRef]
20. Blaht, J.; Balek, J.; Elia, M.; Meletlidis, S. 3D Dilatometer Time-Series Analysis for a Better Understanding of the Dynamics of a Giant Slow-Moving Landslide. *Appl. Sci.* **2020**, *10*, 5469. [CrossRef]
21. Berardino, P.; Fornaro, G.; Lanari, R.; Sansosti, E. A New Algorithm for Surface Deformation Monitoring Based on Small Baseline Differential Sar Interferograms. *IEEE Trans. Geosci. Remote. Sens.* **2002**, *40*, 2375–2383. [CrossRef]
22. Michoud, C.; Baumann, V.; Lauknes, T.R.; Penna, I.; Derron, M.-H.; Jaboyedoff, M. Large slope deformations detection and monitoring along shores of the Potrerillos dam reservoir, Argentina, based on a small-baseline InSAR approach. *Landslides* **2016**, *13*, 451–465. [CrossRef]
23. Aminjafari, S. Monitoring of Masjed-Soleiman embankment dam's deformation using a combination of Interferometric Synthetic Aperture Radar (InSAR) and finite element modeling. *Geod. Cartogr.* **2017**, *43*, 14–21. [CrossRef]
24. Pang, Z.; Jin, Q.; Fan, P.; Jiang, W.; Lv, J.; Zhang, P.; Cui, X.; Zhao, C.; Zhang, Z. Deformation Monitoring and Analysis of Reservoir Dams Based on SBAS-InSAR Technology—Banqiao Reservoir. *Remote Sens.* **2023**, *15*, 3062. [CrossRef]
25. Liao, Z. Study on the Strategic Position and Benefits of Datengxia Water Conservancy Hub. *China Water Resour.* **2020**, *4*, 1–3. (In Chinese)
26. Ansari, H.; De Zan, F.; Parizzi, A. Study of systematic bias in measuring surface deformation with SAR interferometry. *IEEE Trans. Geosci. Remote. Sens.* **2020**, *59*, 1–12. [CrossRef]
27. Ou, Q.; Daout, S.; Weiss, J.R.; Shen, L.; Lazecký, M.; Wright, T.J.; Parsons, B.E. Large-Scale Interseismic Strain Mapping of the NE Tibetan Plateau from Sentinel-1 Interferometry. *JGR Solid Earth* **2022**, *127*, e2022JB024176. [CrossRef]
28. Zhou, L.; Guo, J.; Hu, J.; Li, J.; Xu, Y.; Pan, Y.; Shi, M. Wuhan Surface Subsidence Analysis in 2015-2016 Based on Sentinel-1A Data by SBAS-InSAR. *Remote Sens.* **2017**, *9*, 982. [CrossRef]
29. Wu, W.; Zhou, Z.; Li, T.; Long, S. A Study of Sentinel-1 TOPS Mode Co-registration. *Acta Geod. Cartogr. Sin.* **2017**, *46*, 1156–1164. (In Chinese)
30. Chen, S.; Li, J.; Xie, Y.; Tian, Y. Runoff Inversion in the Li River Basin Based on Sentinel-1 SAR Remote Sensing Images. *People's Pearl River* **2020**, *41*, 116–123.
31. Werner, C.; Wegmuller, U.; Strozzi, T.; Wiesmann, A. Interferometric point target analysis for deformation mapping. In Proceedings of the 2003 IEEE International Geoscience and Remote Sensing Symposium, Toulouse, France, 21–25 July 2003; IEEE: Piscataway, NJ, USA, 2003; Volume 7, pp. 4362–4364.
32. Mora, O.; Mallorquí, J.; Broquetas, A. Linear and nonlinear terrain deformation maps from a reduced set of interferometric SAR images. *IEEE Trans. Geosci. Remote Sens.* **2003**, *41*, 2243–2253. [CrossRef]
33. Hooper, A.; Zebker, H.; Segall, P.; Kampes, B. A New Method for Measuring Deformation on Volcanoes and Other Natural Terrains Using Insar Persistent Scatterers. *Geophys. Res. Lett.* **2004**, *31*, 96–106. [CrossRef]
34. Hooper, A. A multi-temporal InSAR method incorporating both persistent scatterer and small baseline approaches. *Geophys. Res. Lett.* **2008**, *35*, 1–5. [CrossRef]
35. Zhan, W.; Li, Z.; Wei, J.; Zhu, J.; Wang, C. An InSAR Atmospheric Phase Modeling and Estimation Method. *Chin. J. Geophys.* **2015**, *58*, 2320–2329.
36. Doin, M.-P.; Lasserre, C.; Peltzer, G.; Cavalié, O.; Doubre, C. Corrections of stratified tropospheric delays in SAR interferometry: Validation with global atmospheric models. *J. Appl. Geophys.* **2009**, *69*, 35–50. [CrossRef]
37. Hu, Z.; Mallorquí, J.J. An Accurate Method to Correct Atmospheric Phase Delay for InSAR with the ERA5 Global Atmospheric Model. *Remote Sens.* **2019**, *11*, 1969. [CrossRef]
38. Xu, D.; Feng, H.; Yan, S. Time-Series InSAR Analysis of Xiaolangdi Dam Stability Based on Sentinel-1A Images. *China Rural Water Hydropower* **2020**, *6*, 165–170. (In Chinese)
39. Xiao, R.; He, X. Application Research on Time-Series InSAR Deformation Monitoring of Reservoir Dams. *J. Wuhan Univ. (Inf. Sci. Ed.)* **2019**, *44*, 1334–1341. (In Chinese)

40. Pepe, A.; Calò, F. A Review of Interferometric Synthetic Aperture RADAR (InSAR) Multi-Track Approaches for the Retrieval of Earth's Surface Displacements. *Appl. Sci.* **2017**, *7*, 1264. [CrossRef]
41. Gong, C.; Ren, H. Application of Spaceborne Synthetic Aperture Radar in Dam Deformation Monitoring. *China Rural Water Hydropower* **2013**, *2*, 81–84. (In Chinese)
42. Osmanoglu, B.; Sunar, F.; Wdowinski, S.; Cabral-Cano, E. Time series analysis of InSAR data: Methods and trends. *ISPRS J. Photogramm. Remote Sens.* **2016**, *115*, 90–102. [CrossRef]
43. Du, S.; Mallorqui, J.J.; Fan, H.; Zheng, M. Improving PSI Processing of Mining Induced Large Deformations with External Models. *Remote Sens.* **2020**, *12*, 3145. [CrossRef]
44. Emadali, L.; Motagh, M.; Haghighi, M.H. Characterizing post-construction settlement of the Masjed-Soleyman embankment dam, Southwest Iran, using TerraSAR-X SpotLight radar imagery. *Eng. Struct.* **2017**, *143*, 261–273. [CrossRef]
45. Dai, K.; Li, Z.; Tomás, R.; Liu, G.; Yu, B.; Wang, X.; Cheng, H.; Chen, J.; Stockamp, J. Monitoring activity at the Daguangbao mega-landslide (China) using Sentinel-1 TOPS time series interferometry. *Remote Sens. Environ.* **2016**, *186*, 501–513. [CrossRef]